Journal of Alloys and Compounds 867 (2021) 159012

Contents lists available at ScienceDirect

Journal of Alloys and Compounds

journal homepage: www.elsevier.com/locate/jalcom

Transition path to a dense efficient-packed post-delafossite phase. Crystal structure and evolution of the chemical bonding

Raquel Chuliá-Jordán[a], David Santamaria-Perez[a,*], Julio Pellicer-Porres[a], Alberto Otero-de-la-Roza[b], Domingo Martinez-Garcia[a], Braulio Garcia-Domene[a], Oscar Gomis[c], Juan Angel Sans[d], K.A. Vanaja[e], A.S. Asha[f], Catalin Popescu[g]

[a] Departamento de Física Aplicada-ICMUV, Universidad de Valencia, MALTA Consolider Team, E-46100 Burjassot, Valencia, Spain
[b] Departamento de Química Física y Analítica, Facultad de Química, Universidad de Oviedo, MALTA Consolider Team, E-33006 Oviedo, Spain
[c] Centro de Tecnologías Físicas: Acústica, Materiales y Astrofísica, MALTA Consolider Team, Universitat Politècnica de València, 46022 València, Spain
[d] Instituto de Diseño para la Fabricación y Producción Automatizada, MALTA-Consolider Team, Universitat Politécnica de València, E-46022 Valencia, Spain
[e] Department of Chemistry, Maharajas College, Ernakulam, Kochi 682011, Kerala, India
[f] Department of Physics, Cochin University of Science and Technology, Kochi 682022, Kerala, India
[g] CELLS-ALBA Synchrotron Light Facility, 08290 Cerdanyola, Barcelona, Spain

ARTICLE INFO

Article history:
Received 20 October 2020
Received in revised form 29 January 2021
Accepted 30 January 2021
Available online 3 February 2021

Keywords:
Delafossite
High-pressure
Polymorphism
Phase transition
AgGaO2 Structure

ABSTRACT

$A^IB^{III}O_2$ delafossite-type oxides are important technological compounds characterized by the linear coordination of the monovalent *A* metal by oxygen atoms. Based on results of in situ synchrotron X-ray diffraction measurements and ab initio calculations, we herein report on the high-pressure behavior of $AgGaO_2$, to the best of our knowledge the first compound showing step-wise transitions of Ag coordination from linear (2) to octahedral (6), through a leaning delafossite structure. These transformations take place at ~10.5 and ~16.5 GPa, respectively. Our structural analysis evidences that the initial rhombohedral delafossite structure first becomes dynamically unstable, and distorts continuously via a gliding motion of the $[GaO_2]$ octahedral layers within the *ab* plane, and subsequently transform into another rhombohedral phase 8% denser. This structural sequence is associated with a simultaneous decrease in the bond order of the Ag–O bonds and an increase in the ionicity of the crystal. These results may help to unveil the high-pressure phases of several delafossite compounds which were reported to undergo phase transitions under compression that could not be identified.

1. Introduction

The delafossite mineral group is composed of ternary oxides with a general formula $A^IB^{III}O_2$, where *A* is a monovalent noble metal and *B* is a trivalent transition or group 13 metal. Amongst them, those materials having *A* cations with incomplete d orbitals (Pd, Pt) show metallic conductivity and those with a complete d^{10} shell (Cu, Ag) have a semiconducting behavior. This latter type of compounds has been intensively studied after the report of p-type conductivity in transparent $CuAlO_2$ films [1], which together with known n-type transparent conductors [2] could lead to the development of functional windows for optoelectronic applications, like solar panels [3]. These compounds, named transparent conductive oxides, owe their attributes to the fact that metallic d levels and oxygen p levels are energetically close, which lead to an effective orbital hybridization, an increase of the band dispersion and, consequently, an increase of mobility [4]. Besides the combined electrical conductivity and optical properties, these compounds are also used in visible-light-sensitive photocatalysis for hydrogen or chlorine production [5,6], in gas sensors [7] and in ion batteries [8].

The electronic properties of $A^IB^{III}O_2$ materials are intimately related with their chemical bonding. Delafossite oxide crystals can exist as two different polymorphs. The first one is described by the rhombohedral *R*-3*m* space group (Nr. 166) and consists of flat $[BO_2]^-$ octahedral layers stacked in a …ABCABC… conformation with *A* atoms linearly coordinated by O atoms between these layers (see Fig. 1a). The $[BO_6]$ octahedral layers in this polymorph are oriented along the same direction. The second polymorph is described by the hexagonal $P6_3/mmc$ space group (Nr. 194) and consists of similar flat $[BO_6]$ octahedral layers but stacked in a …ABAB… conformation with neighboring layers oriented in opposite directions with respect to

* Corresponding author.
E-mail address: David.Santamaria@uv.es (D. Santamaria-Perez).

https://doi.org/10.1016/j.jallcom.2021.159012
0925-8388/

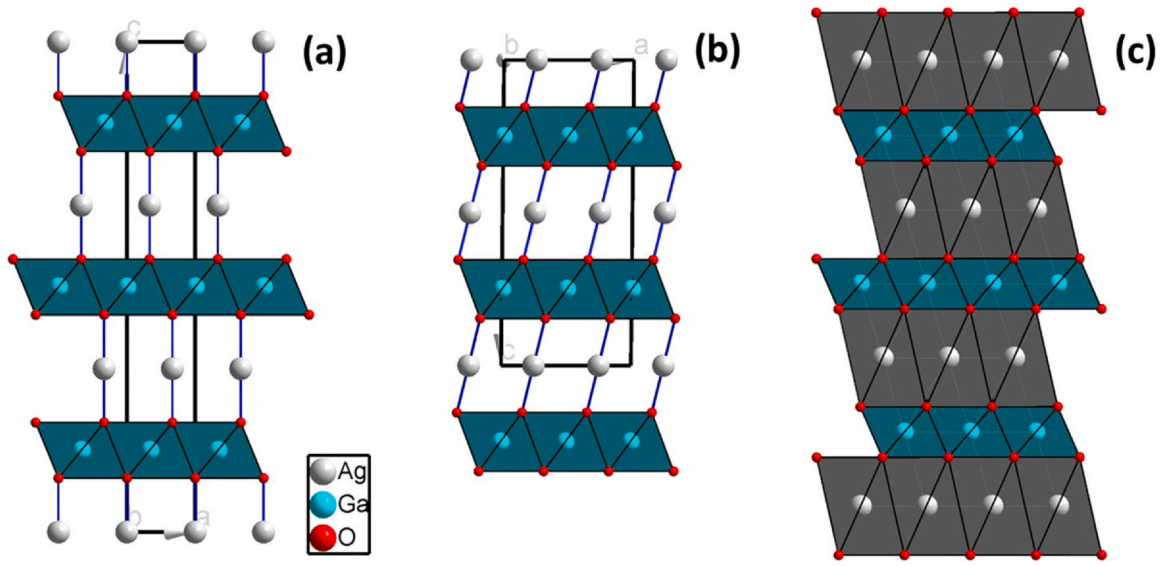

Fig. 1. Crystal structures of (a) the rhombohedral *R*-3*m* Ph1 $AgGaO_2$ delafossite at room pressure, (b) the monoclinic *C*2/*c* Ph2 $AgGaO_2$ at 15.9 GPa, and (c) the rhombohedral *R*-3*m* Ph3 $AgGaO_2$ at 20.4 GPa (right). [GaO_6] octahedra are depicted in cyan, and the Ag and O atoms are represented in gray and red, respectively. Unit-cell edges are shown as solid black lines. In (a) and (b), the Ag–O bonds are depicted as solid blue lines, while in (c) [AgO_6] octahedra are depicted in gray. (For interpretation of the references to color in this figure legend, the reader is referred to the web version of this article.)

one another. The *A* atoms are also linearly coordinated by O atoms between layers. The difference in energy between these two structures is usually very small, which makes that subtle changes in the synthesis' conditions led to the formation of different polytypes [9].

Linear O–*A*–O linkages are due to a strong 3d–4s hybridization of the noble metals [10]. The characteristics of this *A*–O bonding can be finely tuned by the controlled application of external pressures. Hydrostatic compression forces electronic redistribution in solids which may lead to phase transitions to minimize the overall energy of the system [11,12]. Interestingly, copper delafossite structures are characterized by a high axial anisotropy, the c/a ratio increasing with pressure as a consequence of the low compressibility of the O–Cu–O dumbbells [13–21]. Numerous phase transitions in the Cu*B*O_2 (*B* = Al, Ga, In, Sc, Cr, Fe and La) system have been reported [14–24]. However, despite the fact that these studies have good-quality synchrotron XRD data, only the high pressure (HP) phases of $CuFeO_2$ and $CuCrO_2$ have been tentatively determined [18,19]. The structure of the rest of the HP polymorphs remains unknown.

Silver delafossite counterparts have not been studied under compression yet. $AgGaO_2$ is a compound that has been widely studied at ambient conditions [25–29]. Two different polymorphs have been produced by alternative synthesis methods (e.g. cation exchange [26], hydrothermal [27], oxidizing flux [28], ultrasonic-assisted [29] and high-pressure [30] reactions) and characterized at ambient conditions: the above-described rhombohedral delafossite phase (*R*-3*m*, α) and a wurtzite-derived β-$NaFeO_2$-type phase (*Pna*2_1, β) [26]. In the latter phase, both the monovalent and trivalent cations are tetrahedrally coordinated, instead of the two- and six-fold coordination found in delafossite. The resulting packing efficiency is considerably larger in the alpha phase than in the beta phase, as the volume per formula unit shows (V_α/Z_α = 47.8 Å^3, V_β/Z_β = 54.3 Å^3). As far as we know, there is no study of the relative stability of these phases.

Here, we report a joint experimental and theoretical study of the structural stability and polymorphism of $AgGaO_2$ at HP by means of X-ray diffraction (XRD) measurements combined with ab-initio calculations. We will show that the delafossite-type is the thermodynamically stable phase of $AgGaO_2$ at ambient conditions, and that it undergoes two pressure-induced phase transitions at 10.5 and 16.5 GPa, respectively, with a final increase of the coordination number of Ag atoms from 2 to 6 O atoms. The reported structural sequence could help us understand the transformation pathways under compression of a significant number of delafossite-type compounds whose high-pressure phases were not identified in literature [13–17,20,21].

2. Experimental details

The direct synthesis of α-$AgGaO_2$ by conventional solid-state reaction of the constituent oxides at high temperature was not successful. Firstly, sintered disks of β-$AgGaO_2$ were prepared by a two-step process. $NaGaO_2$, which has an orthorhombic structure, was prepared by solid state reaction [31] of stoichiometric amount of Na_2CO_3 and β-Ga_2O_3. The reaction was carried out by successive heating at 650, 750, 850, 1000, and 1050 °C for 24 h at each temperature. The β-$NaGaO_2$ thus obtained is transformed into β-$AgGaO_2$ by reacting with excess molten $AgNO_3$ at 280 °C for 24 h under nitrogen atmosphere. The $AgGaO_2$ obtained through the ion exchange reaction has an orthorhombic *Pna*2_1 structure. The excess $AgNO_3$ was removed by repeated washing with distilled water. The β-$AgGaO_2$ is then converted into α-$AgGaO_2$ by hydrothermal reaction in a Parr bomb at 250 °C. The duration of the reaction was four days. The reagents used were β-$AgGaO_2$ and KOH 1 M solution. The β-$AgGaO_2$ were pelletized by cold isostatic press and then sintered at 350 °C for 5 h in air.

Characterization of the sample at ambient conditions was carried out by energy-dispersive X-ray spectroscopy (EDX) and XRD measurements. Microanalysis was performed with a Hitachi S400 scanning electron microscope and XRD with a Bruker D8 Advance diffractometer using Cu-K_α (1.5406 and 1.5443 Å for $K_{\alpha1}$ and $K_{\alpha2}$, respectively) radiation. Both results confirmed that the sample consisted of 88% $AgGaO_2$ *R*-3*m* delafossite and 12% metallic silver (see Fig. 2).

Powder angle-dispersive HP-XRD measurements were performed up to 20.4 GPa at room temperature in the BL04-MSPD beamline at ALBA synchrotron facility [32]. This beamline is equipped with Kirkpatrick–Baez mirrors to focus the monochromatic beam of wavelength 0.4246 Å down to 20 × 20 μm^2 and with a Rayonix CCD detector with a 165 mm diameter-active area. The detector position and tilts were refined using a reference LaB_6 powder.

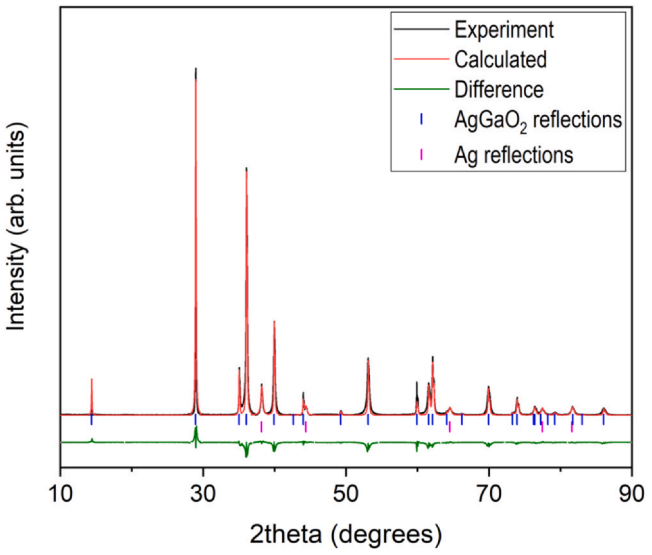

Fig. 2. Observed (black line) and calculated (red line) X-ray diffraction patterns of $AgGaO_2$ delafossite at room conditions ($\lambda_{K\alpha1}$ = 1.5406 Å and $\lambda_{K\alpha2}$ = 1.5443 Å). The green line corresponds to the difference profile between observed and calculated patterns. Vertical blue and magenta marks indicate Bragg reflections of $AgGaO_2$ and Ag, respectively.

XRD patterns collection time was 20 s. The sample and the mixture 16:4:1 methanol:ethanol:water used as pressure transmitting medium were placed in a pressure chamber of 150 μm diameter and 40 μm height inside a diamond-anvil cell. Pressure was determined with the equation of state (EoS) of silver [33]. Integration of 2D diffraction images was performed with Dioptas software [34] while structural analysis was performed by Rietveld and Le Bail refinements using FullProf [35], PowderCell [36] and Unitcell [37] program packages.

3. Computational details

Calculations were carried out using the plane-waves/pseudopotentials method in the projected augmented wave (PAW) framework [38]. We used the Quantum ESPRESSO suite of programs, version 6.5 [39]. The functional used was B86bPBE [40,41] combined with the exchange-hole dipole moment (XDM) method [42–44] to account for dispersion interactions, which has been shown to be important even for solids in which van der Waals interactions are not dominant [45]. A parameter exploration was first carried out, and we determined that plane-wave and density energy cutoffs of 100 Ry and 1000 Ry are enough to give a convergence of 0.1 mRy in the total energy and 0.01 GPa in the pressure. The same criteria were applied for choosing shifted uniform (Monkhorst–Pack) k-point grids. We determined that the optimal grid sizes were 8 × 8 × 1 (*R*-3*m* delafossite, *R*-3*m* α-$NaFeO_2$-type and *P*-3*m* [18]), 8 × 8 × 2 ($P6_3/mmc$ delafossite and *C*2/*m*), 6 × 6 × 2 (*C*2/*c* [18]), and 4 × 4 × 4 ($Pna2_1$, Ref. [26]) for the different structures considered in this study (see later). Geometry relaxations for each phase were carried at zero pressure and 30 GPa using tight convergence criteria (10^{-5} Ry in the energy and 10^{-4} Ry/Bohr in the atomic forces). The equilibrium volumes at these two pressures were used as reference points to build a volume grid with 23 uniformly spaced points spanning the equilibrium volume and the pressure range of interest. At each of these volumes, a constant-volume geometry minimization was carried out in order to find the static equation of state (the energy-volume curve) for each phase. The E(V) data was fitted to a Birch–Murnaghan strain polynomial and the enthalpy, pressure, and stability of each phase was determined using the gibbs2 software [46,47]. Delocalization indices (DI) at all equilibrium geometries of the three relevant phases were calculated using maximally localized Wannier functions calculated using wannier90 [48]. The DIs were computed using a recently described method [49] implemented in the critic2 program [50]. For the DI calculation, we used coarser k-point grids (4 × 4 × 1 for *R*-3*m* delafossite, 3 × 3 × 2 for *C*2/*c*, and 4 × 4 × 2 for α-$NaFeO_2$-type) and a combination of PAW (for the all-electron density) and norm-conserving pseudopotentials, with plane-wave and density cutoffs of 80 and 320 Ry respectively.

Table 1
Lattice parameters and atomic coordinates of the *R*-3*m* delafossite structure (Phase 1) at ambient conditions according to experimental refinement.

Space group: *R*3-*m* (166)
a axis: 2.9887(4) Å
c axis: 18.523(4) Å
Unit-cell volume: 143.29(5) Å^3
Z = 3

	x	y	z
Ag	0	0	0
Ga	0	0	0.5
O	0	0	0.111(2)

4. Results

The structure of the rhombohedral $AgGaO_2$ delafossite is well known. The XRD pattern at room conditions shown in Fig. 2 was refined using the Rietveld method and the rhombohedral *R*-3*m* (space group No. 166) structure reported in literature was used as initial model [51]. The Rietveld refinement yielded the lattice parameters and the atomic coordinates collected in Table 1. Note that all the coordinates are fixed by symmetry except the *z* coordinate of the O atom. Our results agree well with values reported in the literature [51], while the results from our ab-initio calculations overestimate the experimental unit-cell volume by ~4% (see Table 2). The projection of the rhombohedral delafossite along the *b* axis depicted in Fig. 1a shows the …ABCABC… stacking of layers of edge-connected [GaO_6] octahedra and the linear bi-coordination of Ag atoms by O atoms. Linear coordination is frequent among monovalent Group IB chalcogenides [52–55] and the hybridization of s and d_{z^2} orbitals in these metals has been used to explain the linear covalent bonds in Cu^I, Ag^I and Au^I [56]. The Ag–O distances in $AgGaO_2$ delafossite are 2.038 Å, similar to those found in the linear coordination case of Ag_2O silver oxide. It should be also noted that the Ag atoms form hexagonal loosely packed layers of Ag atoms (distances Ag–Ag of 2.989 Å, like the *a* lattice parameter) normal to (001) which resembles the atomic arrangement in the corresponding fcc metal [57,58].

Quasi-hydrostatic pressure generated in a diamond-anvil cell can serve as an effective thermodynamic means to induce electronic redistribution and phase transitions [59,60]. Fig. 3 shows a selection of the XRD patterns of $AgGaO_2$ upon compression. In the diffraction pattern at 1.7 GPa, like in that measured at ambient conditions, all the peaks can be assigned to the title compound except the two peaks that are assigned to elemental silver. This metal has been used as internal gauge to estimate pressure [33]. High-pressure XRD

Table 2
Lattice parameters and atomic coordinates of the *R*-3*m* delafossite structure (Phase 1) at ambient pressure according to theoretical calculations.

Space group: *R*3-*m* (166)
a axis: 3.0282 Å
c axis: 18.7939 Å
Unit-cell volume: 149.25 Å^3
Z = 3

	x	y	z
Ag	0	0	0
Ga	0	0	0.5
O	0	0	0.1129

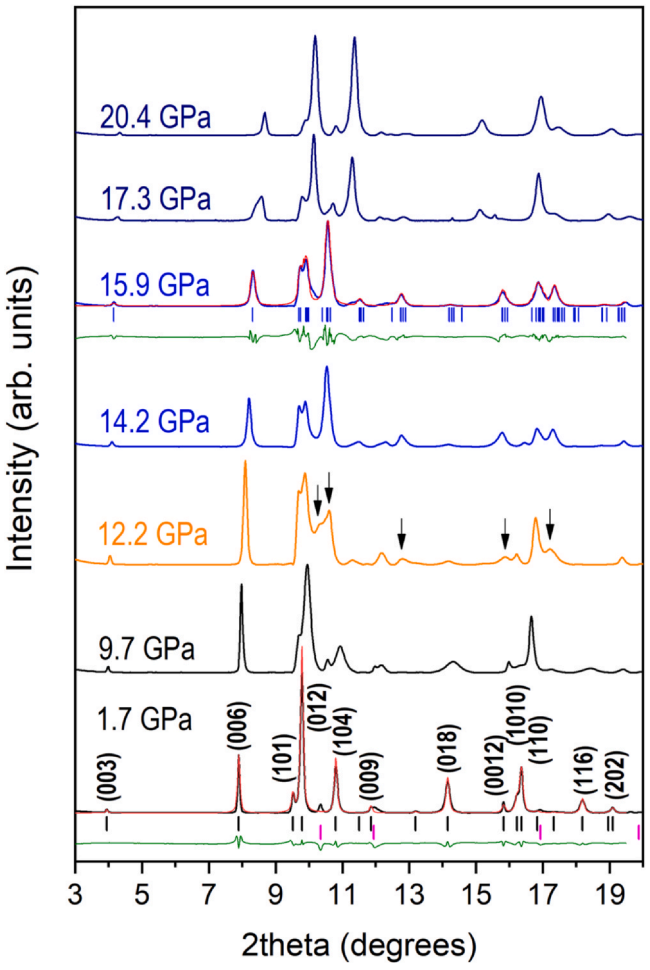

Fig. 3. Selection of room temperature upstroke XRD data of $AgGaO_2$ at different pressures up to 20.4 GPa ($\lambda = 0.4246$ Å). In all diagrams, the background was subtracted. Pressures are indicated in the plot. Patterns corresponding to Ph1, Ph2 and Ph3 $AgGaO_2$ phases are depicted in black, blue and navy, respectively. The arrows in the pattern at 12.2 GPa indicate appearing peaks. In the XRD patterns at 1.7 GPa and 15.9 GPa we show the calculated and difference profiles (red and green lines, respectively). The black, magenta and blue vertical bars indicate the calculated positions of the Bragg reflections of Ph1, Ag (internal pressure marker) and Ph2, respectively.

patterns could be indexed in the initial rhombohedral phase up to 9.7 GPa, but the width of the diffraction peaks varies greatly depending on the reflection. The anisotropic peak broadening becomes evident looking at the (00*l*) reflections, which only broaden moderately with increasing pressure, unlike the rest of reflections. In order to evaluate and better compare the broadening of the different reflections, we have fitted the peak profiles to a pseudo-Voigt function:

$$y = y_0 + A\left[m_u \cdot \frac{2}{\pi} \cdot \frac{w}{4\cdot(x - x_c)^2 + w^2} + (1 - m_u) \cdot \frac{\sqrt{4\cdot ln2}}{\sqrt{\pi}\cdot w} \cdot e^{-\frac{4\cdot ln2\cdot(x-x_c)^2}{w^2}}\right]$$

which is a convolution of Gaussian and Lorentzian functions. The parameters y_0, x_C, A, w and m_u mean the y offset, the peak center, the area, the full width at half maximum (FWHM) and the profile shape factor, respectively. We fixed the contribution of Gaussian and Lorentzian functions to $m_u = 0.7$, after checking experimentally. Fig. 4 shows *hkl*-dependent anisotropic broadening, revealing that the most pronounced broadening occurs for *hkl* reflections with *h* or $k \neq 0$ and simultaneously large *l* indices [61]. The degree of broadening increases upon approaching the first phase transition at 10.5 GPa. Cake images reveal that lattice strains are small in the pressure range of delafossite stability and, therefore, the anisotropic

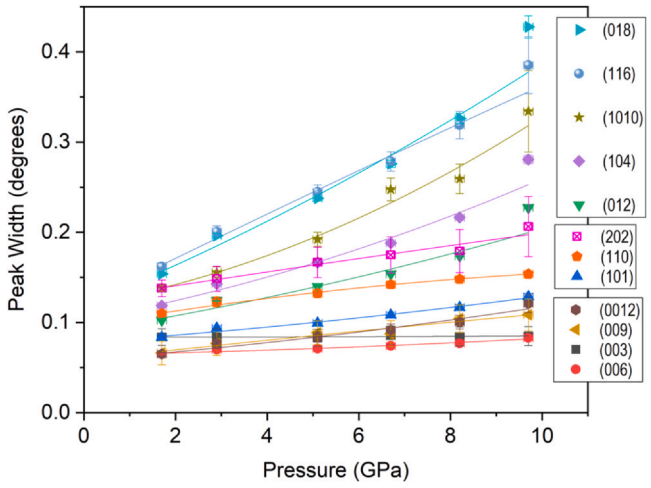

Fig. 4. Evolution of the full width at half maximum (FWHM) of the most intense diffraction peaks of the $AgGaO_2$ delafossite with pressure. Symbols of the different Bragg reflections indicated at the right hand side.

peak broadening was attributed to stacking faults of this layered compound [62].

The obtained evolution for the unit-cell volume and lattice parameters of the initial low-pressure delafossite phase of $AgGaO_2$, hereafter denoted as Ph1, are collected in Table 3 and shown in Fig. 5. A third-order Birch–Murnaghan equation of state (EOS) was used to fit our pressure–volume data [63]. As we only have six P–V data points of the Ph1 phase, we decided to fix the first pressure derivative of the bulk modulus to our calculated value ($B'_0 = 4.47$). We obtained an experimental bulk modulus for the initial delafossite phase of $B_0 = 169(3)$ GPa, and a zero-pressure volume of $V_0 = 144.08(7)$ Å^3, which agree well with our ambient conditions measurement. Theoretical calculations yield a larger V_0 value, 149.22 Å^3, and smaller bulk modulus, $B_0 = 140.7$ GPa, likely due to a combination of factors: (i) few P–V experimental datapoints, (ii) inaccurate DFT description [45,54], and (iii) role of thermal effects. These results show that the $AgGaO_2$ delafossite is considerably more compressible than its copper counterpart. Compare, for instance, the measured $CuGaO_2$ bulk modulus $B_0 = 202(15)$ GPa obtained fixing $B'_0 = 3.9$ [15] with the $AgGaO_2$ $B_0 = 172(3)$ GPa when our data are fitted with the same B'_0. Fig. 5 shows that the contraction of the lattice parameters is rather anisotropic. For instance, according to our experiments, the relative contractions for *a* and *c* between 1.7 and 9.7 GPa are 1.59% and 0.94%, respectively. An analysis in terms of linear axial compressibilities (β) of our delafossite structure yields $\beta_a = 2.01(3)\cdot10^{-3}$ GPa^{-1} and $\beta_c = 1.14(3)\cdot10^{-3}$ GPa^{-1}. As can be seen in Fig. 5, the relative axial compression of the unit-cell axes predicted by our calculations show a good agreement with our experimental data ($\beta_a = 2.39(6)\cdot10^{-3}$ GPa^{-1} and $\beta_c = 1.17(3)\cdot10^{-3}$ GPa^{-1}). The compressibility of the *a* axis is similar to those reported for copper delafossites ($1.96(5)\cdot10^{-3}$ and $2.06(5)\cdot10^{-3}$ GPa^{-1} for $CuGaO_2$ and $CuAlO_2$, respectively), but the *c* axis of $AgGaO_2$ is significantly more

Table 3
Experimental lattice parameters of the *R*-3*m* delafossite structure (Phase 1) at high pressures. Up and down indicates upstroke and downstroke compression data.

Pressure (GPa)	*a* axis (Å)	*c* axis (Å)	Unit-cell volume (Å^3)
1.7 (up)	2.9846(5)	18.505(4)	142.76(5)
2.9 (up)	2.9764(5)	18.470(4)	141.70(5)
5.1 (up)	2.9622(4)	18.425(4)	140.02(5)
6.7 (up)	2.9527(4)	18.395(4)	138.90(5)
8.2 (up)	2.9440(6)	18.365(4)	137.84(6)
9.7 (up)	2.9370(6)	18.331(4)	136.96(6)
8.1 (down)	2.9445(4)	18.303(4)	137.43(5)
10^{-4} (down)	2.9853(5)	18.495(4)	142.74(5)

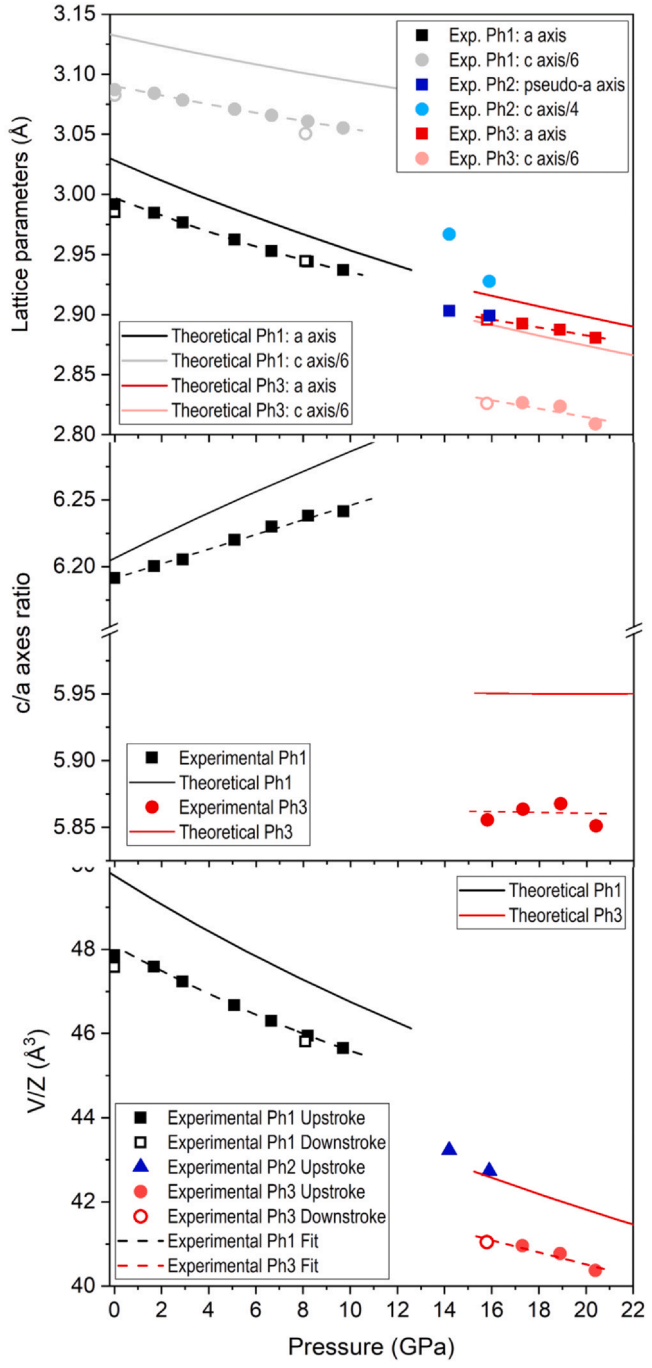

Fig. 5. (Top) Pressure dependence of the lattice parameters *a* (squares) and *c*/6 (circles) of Ph1 (black and gray symbols) and Ph3 (red and pink symbols) $AgGaO_2$ phases. Solid and empty symbols correspond to upstroke and downstroke data, respectively. Dashed and solid lines are fits to the experimental and theoretical data, respectively. Pseudo-hexagonal axes of Ph2, defined as $\boldsymbol{a}' \sim \boldsymbol{a} + \boldsymbol{b}/2$, $\boldsymbol{a}' \sim \boldsymbol{b}$, $\boldsymbol{c}' \sim \boldsymbol{c}$ from the monoclinic axes, are also included. (Center) *c*/*a* axes ratio of Ph1 and Ph3 according to experiments and calculations. (Bottom) Pressure dependence of the volume per formula unit of the different $AgGaO_2$ phases: Ph1 (black squares), Ph2 (Blue triangles) and Ph3 (red circles). Experimental upstroke and downstroke data are depicted as solid and empty symbols, respectively. Experimental and theoretical EOS fittings are represented as dashed and solid lines. (For interpretation of the references to color in this figure legend, the reader is referred to the web version of this article.)

compressible $(0.75(4)\cdot10^{-3}$ and $0.83(4)\cdot10^{-3}$ GPa^{-1} for $CuGaO_2$ and $CuAlO_2$, respectively) [14,15]. The anisotropy entails an increase of the *c*/*a* axes ratio with increasing pressure according to the expression $c/a = 6.191(2) + 0.0055(3)\cdot P$. This response to external pressure arises from the fact that the relatively incompressible linear O–Ag–O bonds are along the *c* direction, whereas the compressibility of the *a* axis is directly attributable to the compression of $[GaO_6]$ octahedra, which tend to become more regular under high pressure [14,15].

Above 9.7 GPa additional diffraction peaks appear, which indicates the existence of a structural phase transition at this pressure (see Fig. 3). The XRD patterns measured in the pressure range between 10 and 14 GPa could not be indexed. At 14.2 and 15.9 GPa, the 10 most intense diffraction peaks were initially indexed with a hexagonal lattice. At 15.9 GPa, the indexed hexagonal parameters were $a = 2.903(2)$ Å and $c = 11.72(2)$ Å. As it can be noted, the *c* axis of this cell is approximately 2/3 of that of the delafossite Ph1 phase. These dimensions are similar to those of (i) the *P*-3*m* phase suggested by Xu et al. for the second HP $CuFeO_2$ polymorph [18], which would be characterized by Ag atom in tetrahedral coordination, and (ii) the $P6_3/mmc$ $AgFeO_2$-type phase, the hexagonal delafossite polytype, where Ag atoms are still bicoordinated, forming "dumbbells" [64]. However, these atomic arrangements did not explain satisfactorily the observed diffraction intensities. The leaning delafossite structure described within the *C*2/*c* space group by Xu et al. for the first high-pressure phase of $CuFeO_2$ [18] reproduce slightly better the intensities of the experimental XRD pattern (lattice constants at 15.9 GPa collected in Table 4). The XRD pattern is shown in Fig. 3 together with the LeBail refinement. Like *R*-3*m* Ph1, the *C*2/*c* Ph2 phase is a layered structure with octahedral $[GaO_2]^-$ layers but now they stacked in approximately …ABAB… configuration (monoclinic β angle of 90.59°) as can be seen in Fig. 1b. The linear coordination of Ag atoms in Ph1 would be preserved with the dumbbells forming an angle of ~12.3° relative to the *c* axis. The Ag–O distances would be ~1.96 Å. Theoretical calculations confirm that a *C*2/*c* phase whose atomic arrangement slightly differs from that suggested above becomes energetically favorable above 14.7 GPa (see calculated cell dimensions and atomic coordinates in Table 5 and the visual representation in Fig. 6). Our calculations find energetically favorable at this pressure a structure with a monoclinic β angle of 97.9°, but O–Ag–O dumbbells perpendicular to the $[GaO_2]^-$ layers. Figs. 1b and 6 show that the experimental and theoretical *C*2/*c* structures are related through a gliding movement of the different layers. Lattice parameters overestimation in theoretical simulations entails overestimated Ag–O distances in dumbbells (2.115 Å).

The Ph2 phase is stable up to about 16.5 GPa, where another transition takes place (see Fig. 3). At 17.3 GPa, all the diffraction peaks correspond to the high-pressure Ph3 phase. Note that the peak widths of Ph3 are quite uniform even at these high pressures, not showing evidence of any *hkl* dependence. The peaks of the XRD pattern at 20.4 GPa, the maximum pressure reached in this study, were indexed on the basis of a rhombohedral cell with the lattice parameters collected in Table 6. The intensities of the diffraction peaks match to those of a α-$NaFeO_2$-type structure described with a *R*-3*m* space group, which is basically a rocksalt superstructure where Ag and Ga atoms are ordered. The Rietveld refinement of the limited-quality XRD pattern is shown in Fig. 7 together with the calculated and difference profiles. Both the refined lattice and atomic

Table 4
Lattice parameters of the *C*2/*c* intermediate structure (Phase 2) at 15.9 GPa according to experimental refinement. We include the atomic coordinates reported by Xu et al. for the first high-pressure phase of $CuFeO_2$ described within the same space group [18].

Space group: *C*2/*c* (15)
a axis: 4.999(1) Å
b axis: 2.907(1) Å
c axis: 11.710(4) Å
β angle: 90.5(1)°
Unit-cell volume: 170.9(2) $Å^3$
Z = 4

	x	y	z
Ag	0.75	0.75	0
Ga	0.5	0	0.25
O	0.336	0.536	0.154

Table 5
Lattice parameters and atomic coordinates of the *C*2/*c* intermediate structure (Phase 2) at 15.9 GPa according to theoretical calculations.

Space group: *C*2/*c* (15)
a axis: 5.2258 Å
b axis: 3.0179 Å
c axis: 12.6283 Å
β angle: 97.94°
Unit-cell volume: 197.26 Å^3
Z = 4

	x	y	z
Ag	0.75	0.75	0
Ga	0.5	0.75	0.25
O	0.3063	0.25	0.1691

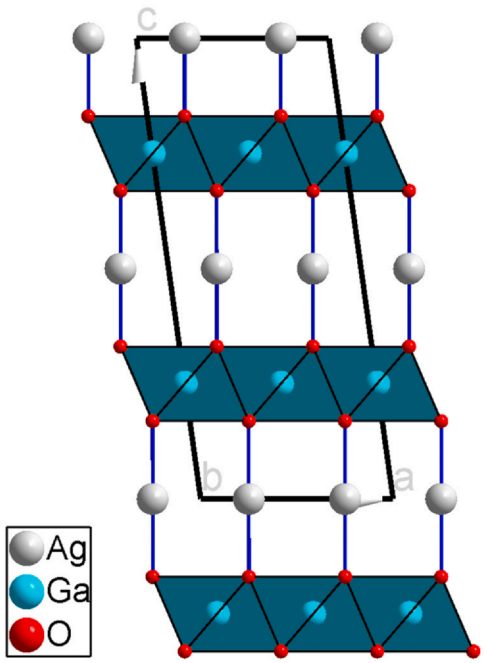

Fig. 6. Projection of the calculated monoclinic *C*2/*c* structure at 15.9 GPa, to be compared to the suggested experimental one depicted in Fig. 1b. [GaO_6] octahedra are depicted in cyan, and the Ag and O atoms are represented in gray and red, respectively. Ag–O bonds are depicted as solid blue lines and the unit-cell edges as solid black lines. (For interpretation of the references to color in this figure legend, the reader is referred to the web version of this article.)

Table 6
Lattice parameters and atomic coordinates of the *R*-3*m* α-$NaFeO_2$-type structure (Phase 3) at 20.4 GPa according to experimental refinement.

Space group: *R*3-*m* (166)
a axis: 2.8805(5) Å
c axis: 16.854(5) Å
Unit-cell volume: 121.11(4) Å^3
Z = 3

	x	y	z
Ag	0	0	0
Ga	0	0	0.5
O	0.6666	0.3333	0.107(6)

parameters are in good agreement with those theoretically calculated (see Table 7). This Ph3 structure is represented in Fig. 1c, together with the other two phases of $AgGaO_2$. The *a* axis barely decreases compared to the Ph1 phase, but the *c* axis suffers a collapse of 6.5% (see Fig. 5). This change in unit-cell dimensions is determined by the limitation in Ag–Ag distances within the *ab* plane and the Ag coordination increase from 2 to 6 O atoms, which entails the shortening of the *c* axis. The Ag–O distances within the first-coordination sphere increase (6 × 2.48 Å at 20.4 GPa) due to this increase in the Ag coordination number.

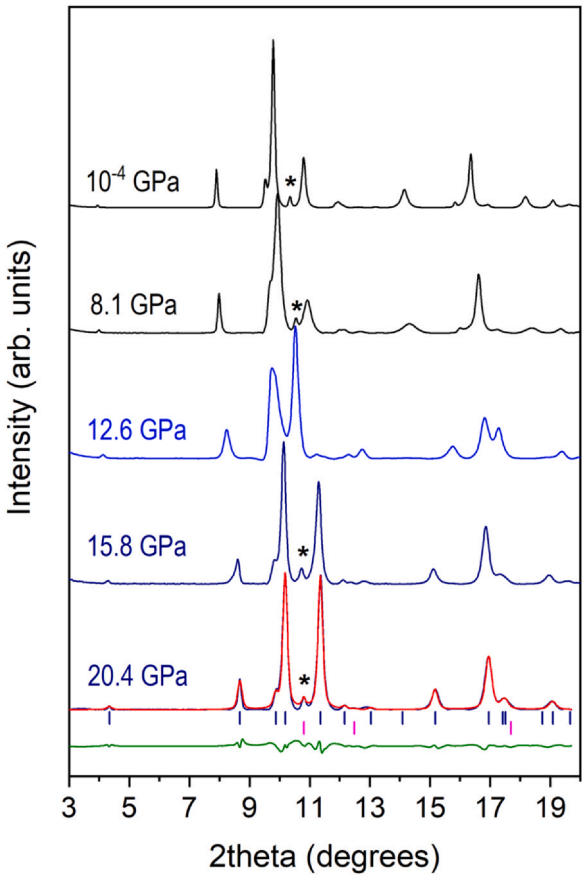

Fig. 7. Selection of room temperature downstroke XRD data of $AgGaO_2$ at different pressures from 20.4 GPa to room pressure (λ = 0.4246 Å). In all diagrams, the background was subtracted. Pressures are indicated in the plot. Patterns corresponding to Ph1, Ph2 and Ph3 $AgGaO_2$ phases are depicted in black, blue and navy, respectively. In the XRD pattern at 20.4 GPa we show the calculated and difference profiles (red and green lines, respectively). The vertical bars and Miller indexes indicate the calculated positions of the Bragg reflections. The asterisk marks the (111) reflection of metallic silver.

Table 7
Lattice parameters and atomic coordinates of the *R*-3*m* α-$NaFeO_2$-type structure (Phase 3) at 20.4 GPa according to theoretical calculations.

Space group: *R*3-*m* (166)
a axis: 2.8966 Å
c axis: 17.2352 Å
Unit-cell volume: 125.24 Å^3
Z = 3

	x	y	z
Ag	0	0	0
Ga	0	0	0.5
O	0.6666	0.3333	0.1054

Fig. 5 also shows the pressure dependence of the unit-cell volumes of the $AgGaO_2$ rocksalt superstructure Ph3 phase. The experimental P–V results of the Ph3 phase could not be fitted using a third order Birch–Murnaghan EOS because of insufficient data. However, a linear fit of our 4 data (collected in Table 8) shows that this high-pressure phase is less compressible than the initial delafossite structure. The theoretically calculated P–V data points of this phase were fitted to obtain the ambient pressure bulk modulus B_0 = 141.8(2) GPa, its first derivative $B_{0'}$ = 4.81(1), and the ambient pressure unit-cell volume V_0 = 139.82(1) Å^3. As can be seen, according to calculations, the Ph3 phase has a bulk modulus similar to that of the Ph1 phase, but the high-pressure phase becomes more incompressible with increasing pressure ($B_{0'Ph3} > B_{0'Ph1}$). The difference between the calculated unit-cell volumes of both phases is

Table 8
Experimental lattice parameters of the *R*-3*m* α-$NaFeO_2$-type structure (Phase 3) at high pressures. Up and down indicates upstroke and downstroke compression data.

Pressure (GPa)	*a* axis (Å)	*c* axis (Å)	Unit-cell volume (Å^3)
17.3 (up)	2.8924(6)	16.960(7)	122.88(5)
18.9 (up)	2.8873(5)	16.942(5)	122.32(4)
20.4 (up)	2.8805(5)	16.854(5)	121.11(4)
15.8 (down)	2.8957(5)	16.956(5)	123.13(4)

6.2%, in good agreement with experimental results. As shown in Fig. 7, the initial delafossite-type phase is recovered after decompression. It should be also mentioned that the c axis of the delafossite-type phase during decompression is ~ 0.2% smaller than that upon compression. The interlayer distances do not recover the initial values. After two phase transitions with a 6.3% volume collapse, the recovered initial structure must be considerably stressed during the downstroke process, a fact that is reflected in a larger peak broadening in decompression XRD patterns. We speculate that this could be the reason for the observed discrepancy in c axis values.

Several phases were considered as potential thermodynamically stable polymorphs in our DFT calculations (see Fig. 8a). These phases correspond to the initial *R*-3*m* Ph1 delafossite structure, the wurtzite-derived *Pna*2$_1$ phase of $AgGaO_2$ [26], the monoclinic *C*2/*m* structure from *R*-3*m* distortion, the *C*2/*c* reported by Xu et al. for the first HP phase of $CuFeO_2$ [18], the hexagonal *P*-3*m* phase with tetra-coordinated Ag atoms reported by Xu et al. for the second HP phase of $CuFeO_2$ [18], the hexagonal *P*6$_3$/*mmc* $AgFeO_2$-type delafossite [64] and the rhombohedral *R*-3*m* α-$NaFeO_2$-type Ph3 structure. The calculations show that the wurtzite-derived *Pna*2$_1$ phase would be thermodynamically stable at negative pressures (large volumes) and that the rhombohedral *R*-3*m* and the hexagonal *P*6$_3$/*mmc* delafossite polytypes are energetically similar, being the *R*-3*m* structure the thermodynamically stable phase at ambient pressure. The stability of the *R*-3*m* delafossite phase respect to the *Pna*2$_1$ phase is supported by the observed transition to the *R*-3*m* phase when a sample in the *Pna*2$_1$ phase is dissolved in water [65]. From the enthalpy difference–pressure curves (Fig. 8b), we find that rhombohedral delafossite becomes energetically unfavorable against its *C*2/*m* monoclinic distortion above 14.7 GPa. The variant of the *C*2/*c* structure reported by Xu et al. for the first HP phase of $CuFeO_2$ is energetically more stable than the initial *R*-3*m* and *C*2/*m* phases above 13 GPa. The other $CuFeO_2$ high-pressure structure reported by Xu et al., consisting of tetra-coordinated Ag atoms, is not competitive with the aforementioned phases in the whole pressure range. A second structural transition was found at 30.5 GPa to the α-$NaFeO_2$-type *R*-3*m* phase. This transition pressure is significantly higher than that observed experimentally (16.5 GPa).

The observed experimental sequence entails a progressive relative gliding of the Ag^+ and $[GaO_2]^-$ layers upon compression, which has a direct effect on the number of neighboring O atoms surrounding Ag atoms in the first and second coordination spheres. Silver in $AgGaO_2$ delafossite is linearly coordinated by oxygen but it has 12 additional second-neighbor distances (2 × 2.03 Å + 12 × 3.61 Å at 1.7 GPa, for instance). After the first HP phase transition to the *C*2/*c* structure, the Ag atoms are still bi-coordinated. However, the relative gliding displacement between the atomic layers causes the shortening of some of the Ag–O distances of the second coordination sphere (2 × 1.94 Å + 2 × 2.85 Å + 2 × 2.94 Å + 2 × 3.42 Å + 2 × 3.55 Å at 15.9 GPa). The transformation into the *R*-3*m* α-$NaFeO_2$ structure implies an octahedral coordination of next O neighbors (6 × 2.48 Å at 20.4 GPa) and eight Ag–O longer distances (2 × 3.77 Å + 6 × 3.81 Å) that form the second coordination sphere. This latter high-pressure phase is described with the same space group as the initial delafossite phase, the position of the Ag and Ga atoms remains the same, but the O atoms have migrated (*a*/3, *b*/3) which entail a displacement of ~1.7 Å and the increase of the Ag coordination number from 2 to 6.

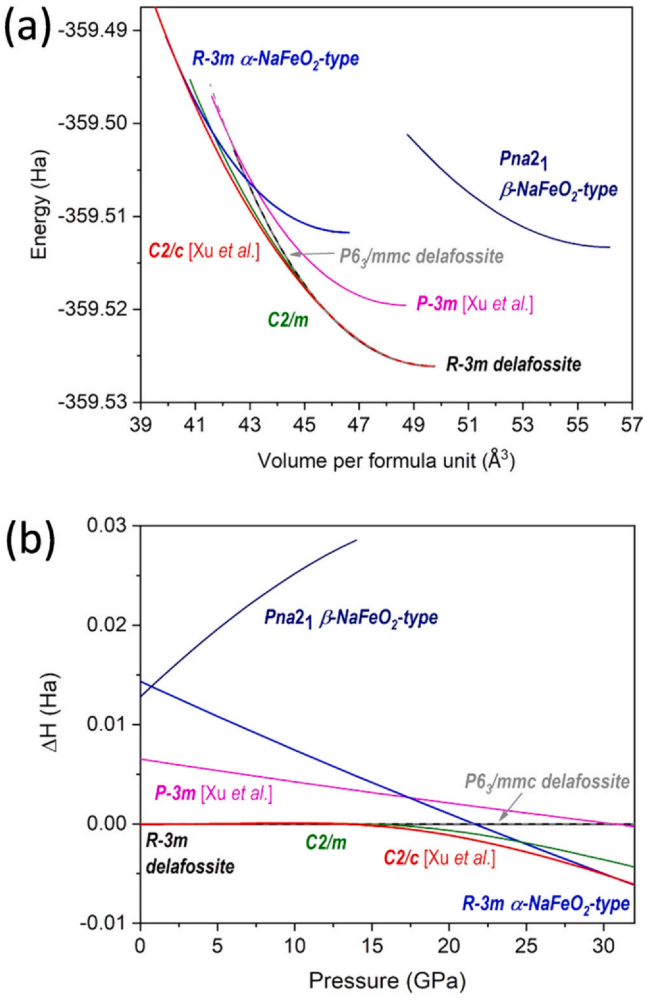

Fig. 8. Theoretical calculation of (a) energy vs volume and (b) enthalpy difference vs pressure for the following potential phases of $AgGaO_2$: the *R*-3*m delafossite*, the *C*2/*m* phase from *R*-3*m* distortion, the *C*2/*c* phase reported by Xu et al. for the first HP polymorph of $CuFeO_2$ [18], the hexagonal *P*-3*m* phase with tetra-coordinated Ag atoms reported by Xu et al. for the second HP polymorph of $CuFeO_2$ [18], the hexagonal *P*6$_3$/*mmc* $AgFeO_2$-type delafossite [60] and the rhombohedral *R*-3*m* α-$NaFeO_2$-type Ph3 phase. Enthalpy of *R*-3*m* delafossite phase is taken as the reference in (b).

Our calculations can be used to analyze the behavior of $AgGaO_2$ under pressure and the evolution of bonding in this material. Fig. 9(a–c) shows the evolution of the atomic charges with pressure in this system [50,66]. As expected, $AgGaO_2$ at ambient pressure has a partial ionic character with charges of +0.48 (Ag), +1.62 (Ga), and −1.05 (O). These charges evolve under compression differently. The charge in Ga slowly decreases with pressure, regardless of the phase. However, there are significant differences in the behavior of Ag and O charges in the intermediate Ph2 (*C*2/*c*) phase compared to the other two. While the charge of Ag is mostly constant in Ph1 and Ph3, it increases significantly with pressure in Ph2, indicating an evolution of this system towards higher ionicity and lower covalency under compression. The evolution of the O atomic charge follows a similar, but opposite, trend.

The increase in ionicity is reasonable given that the Ag–O coordination evolves from two-fold in Ph1 to 2 + 4 in Ph2 and finally to a six-fold coordination in Ph3. The degree of electron sharing in Ag–O bonds can be estimated by calculating the Bader localization and delocalization indices at each pressure [66,67]. Atomic delocalization values (average number of electrons, N, minus localization

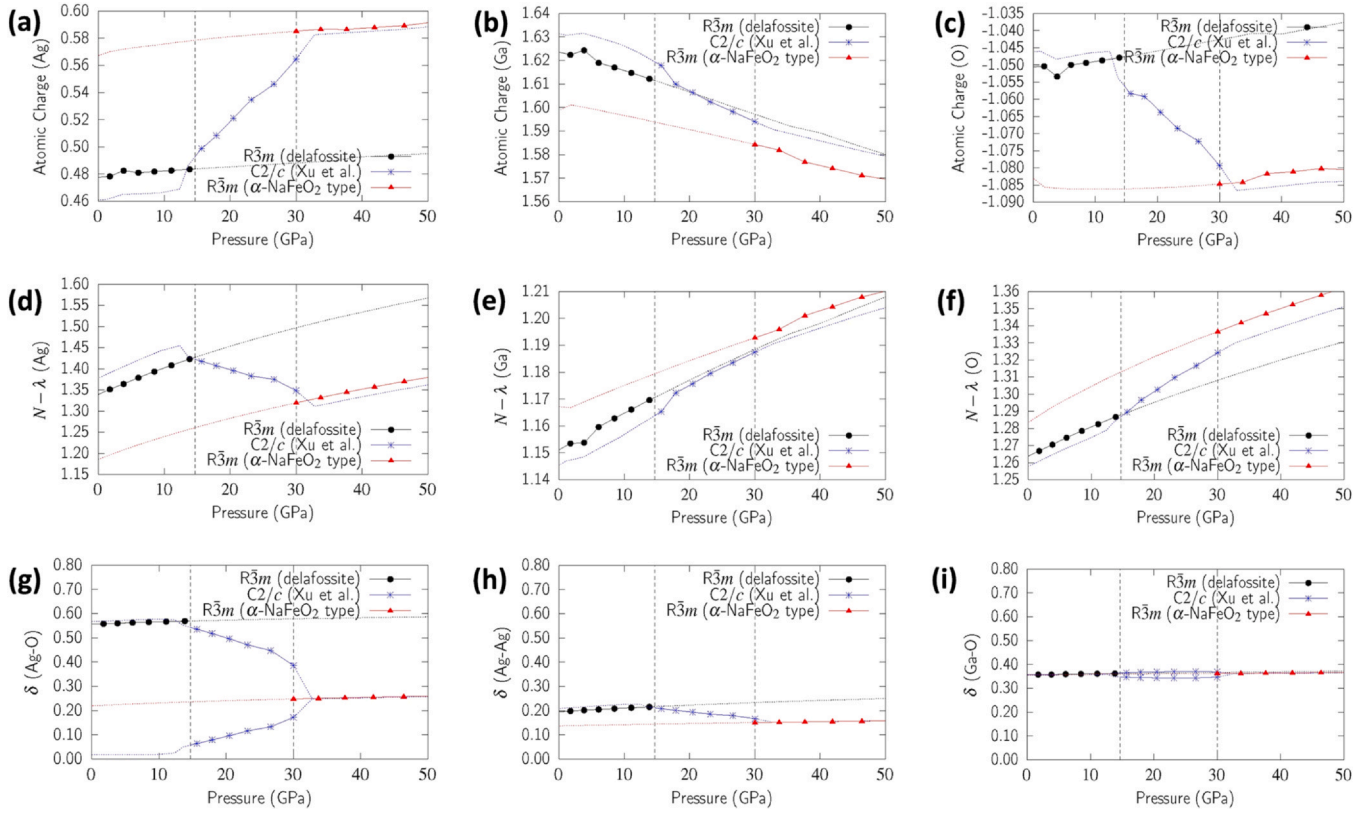

Fig. 9. Caption: Integrated atomic properties as a function of pressure: charge in Ag (a), Ga (b), and O (c); electron delocalization (equal to the average number of electrons minus the localization index) in Ag (d), Ga (e), and O (f); delocalization indices between nearest neighbors in Ag–O pairs (g), Ag–Ag (h), and Ga–O (i). Values for the *R*-3*m* delafossite (black), *C*2/*c* (blue), and *R*-3*m* α-$NaFeO_2$-type (red) phases are given, with approximate transition pressures indicated by vertical lines. Full lines are used inside the domain of stability of each phase. For the *C*2/*c* phase, the first and second-neighbor Ag–O and Ga–O contacts are shown. (For interpretation of the references to color in this figure legend, the reader is referred to the web version of this article.)

index, lambda) for each atom are shown in Fig. 9(d–f). Application of pressure typically induces an increase in the number of delocalized electrons that is proportional to the volume compression, and this is confirmed by the figures. The exception is the Ag atom in Ph2, which shows an atypical decrease in the number of delocalized electrons with pressure, again indicative of the evolution from a covalent to an ionic bonding scenario.

Delocalization indices for nearest-neighbor Ag–O, Ag–Ag, and Ga–O contacts are shown in Fig. 9(g–i). The Ga–O and Ag–Ag DIs are relatively unaffected by pressure. The former indicates a degree of covalency in the bonding between Ga and O, while the significant Ag–Ag DI may point to the existence of metallophilic interactions in this system. Indeed, the evolution of the Ag–Ag distance under compression is shown in Fig. 10(b). Even at zero pressure, the Ag–Ag distance is well below twice the van der Waals radius of silver (2 × 1.72 Å [68] = 3.44 Å). This observation, combined with the relatively high DI value indicates a contribution to binding from Ag-Ag interactions, which, being dispersion dominated [69], increase under compression as the Ag–Ag distance decreases. The Ag–O delocalization indices reproduce almost exactly the change in coordination under compression in this system. In Ph1, Ag is coordinated to two oxygen at a DI more than 0.5, a significantly covalent polar bond. In Ph2, Ag has a 4 + 2 coordination. The DIs for the incipient Ag–O bonds increase, and the DIs for the short Ag–O bonds decrease. At the transition pressure to Ph3, these two DIs merge and the system acquires a sixfold Ag–O coordination with predominantly polar bonds. We note that, contrary to the Ag–O bonds, the Ga–O and Ag–Ag DIs do not mimic the evolution of the corresponding interatomic distances, as shown in Fig. 10(a, c). This indicates that those atomic interactions are mostly unaffected by pressure.

To complete our bonding analysis, Fig. 11 shows the total and partial density of states (DOS) for the three phases within their calculated domain of stability. The ambient-pressure DOS for the Ph1 phase agrees with the one reported in Ref. [10]. The Ga energy levels are relatively low in energy and the conduction band is dominated by the Ag(p) and O(p) levels. In the Ph1 phase, there is significant hybridization between the Ag(d) levels and the O(p) levels, consistent with the formation of partially covalent bonds. The O(p) are higher in energy than Ag(d). As pressure increases, the regions corresponding to the Ag(d) and O(p) energy levels widen until, they overlap in Ph3, reflecting the increase number of O atoms around a given Ag atom.

$AgGaO_2$ does not follow the same trend in terms of phase transition sequence as Cu(Fe, Mn, Cr)O_2 [18,19]. This is not surprising since in the latter compounds the structural modifications could depend on the valence exchange and the magnetic properties. As far as we know, the structural sequence observed in $AgGaO_2$ has never been reported and provides a plausible transformation pathway for (i) copper delafossite compounds whose studies reported phase transitions but the high-pressure phases were not determined, or (ii) the silver delafossite-type compounds that have not been studied under compression. Cu delafossites of Al, Ga, La and Sc, for instance, transform to unresolved structures. XRD and Raman spectroscopy measurements on $CuAlO_2$ and $CuGaO_2$ evidenced structural transformations at 34 and 26 GPa, respectively, and extended-ray absorption fine structure (EXAFS) measurements confirmed that the transition involves a change in copper environment [14,15,22,23]. Optical absorption results and ab initio calculations on $CuScO_2$ showed an abrupt discontinuity in the bandgap behavior at 18 GPa, which suggested that a phase transition took place at that pressure [16]. La atoms have larger atomic radii than Sc, Ga or Al atoms and, therefore, phase transitions

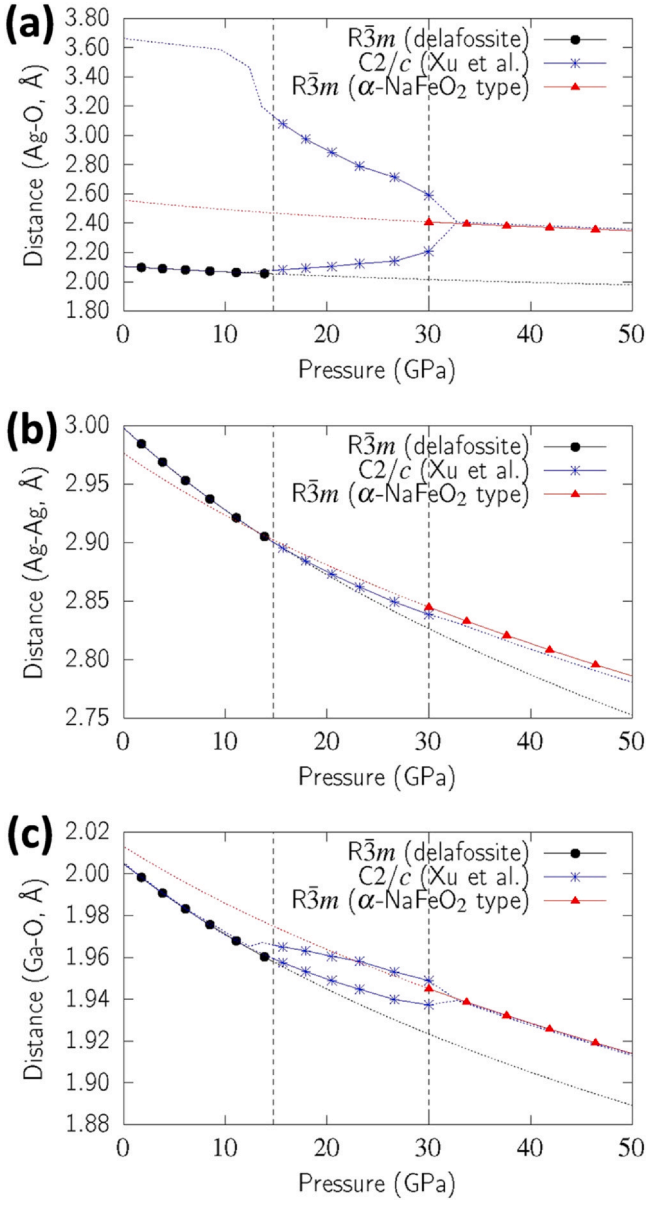

Fig. 10. Nearest-neighbor interatomic distances as a function of pressure for Ag–O pairs (a), Ag–Ag (b), and Ga–O (c). Values for the *R*-3*m* delafossite (black), *C*2/*c* (blue), and α-$NaFeO_2$-type (red) phases are given, with approximate transition pressures indicated by vertical lines. Full lines are used inside the domain of stability of each phase. For the *C*2/*c* phase, the first and second-neighbor Ag–O and Ga–O contacts are shown. (For interpretation of the references to color in this figure legend, the reader is referred to the web version of this article.)

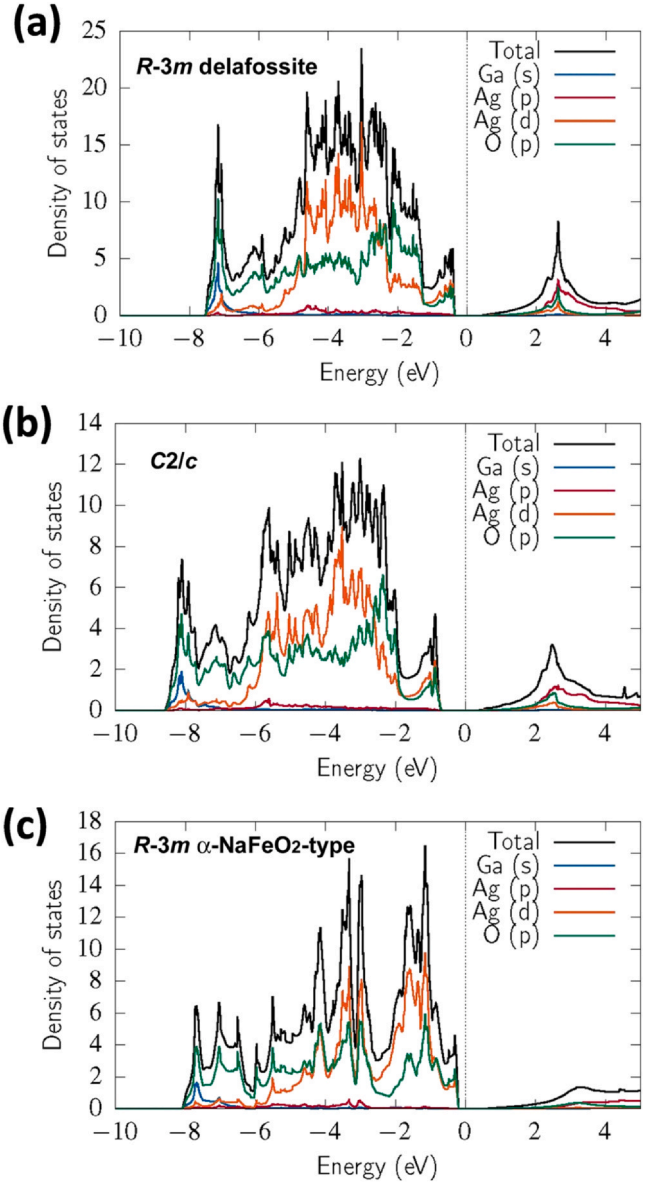

Fig. 11. Calculated total and partial density of states in *R*-3*m* delafossite (a), *C*2/*c* (b), and α-$NaFeO_2$-type (c) phases. The Fermi level is at zero energy.

in $CuLaO_2$ are expected to occur at lower pressures than the others [70]. This was confirmed by Raman spectroscopy, electrical resistance and XRD techniques, that indicated that two phase transitions occur at 1.8 and 7 GPa [20]. Like in the previous cases, the structure of the high-pressure polymorphs could not be determined. We expect our results could be a reference for future structural analyses of delafossite compounds under compression.

5. Conclusions

Linear coordination is characteristic of group 11 compounds. Copper and silver delafossites present it (O–Cu/Ag–O dumbells) due to a 3d–4s hybridization of the monovalent metal orbitals. The behavior of these compounds under compression is poorly known. In this work, we report the first high-pressure study of a silver delafossite. We have studied the high-pressure structural stability of $AgGaO_2$ rhombohedral delafossite by means of synchrotron X-ray diffraction experiments that have been complemented with ab initio total-energy calculations. We have experimentally (theoretically) found that the compression induces two phase transitions at 10.5 (14.7) and 16.5 (30.5) GPa, from the *R*-3*m* delafossite through a monoclinic *C*2/*c* to another rhombohedral *R*-3*m* phase, which can be described as an α-$NaFeO_2$-type structure with the Ag atoms in octahedral coordination. This structural sequence shows that the NaCl-like AgGa cation subarray remains basically immovable [71] and the oxygen layers glide in such a way that the atomic migration produces an increase of Ag coordination and a more efficient packing. The observed phase transitions involve a total volume collapse of approximately 6.3%. From our data, we have also determined the equations of state and axial anisotropy for the two rhombohedral polymorphs. $AgGaO_2$ delafossite has smaller bulk modulus than its copper counterpart due to more compressible *A*–O bonds. However, O–Ag–O dumbells aligned along the *c* direction are relatively incompressible compared to the [GaO_6] octahedra, which results in an increase of the *c*/*a* axes ratio with increasing pressure. We show that

the increase in Ag–O coordination is related to an increase in the ionicity of the crystal and the disappearance of the covalent character that these bonds have at ambient pressure.

In summary, we have presented a consistent joint experimental and theoretical picture of the high-pressure behavior of the silver gallium delafossite, which could be used as a reference to identify dense $CuBO_2$ polymorphs previously found in literature, but not solved. The nature of the electronic changes in the Ag–O bonds were also unveiled.

CRediT authorship contribution statement

Raquel Chuliá-Jordán: Formal analysis, Writing - original draft, Writing - review & editing. **David Santamaria-Perez**: Conceptualization, Investigation, Formal analysis, Writing – original draft, Writing - review & editing. **Julio Pellicer-Porres**: Conceptualization, Formal analysis, Writing - review & editing. **Alberto Otero-de-la-Roza**: Investigation, Formal analysis, Writing - review & editing. **Domingo Martinez-Garcia**: Investigation, Writing - review & editing. **Braulio Garcia-Domene**: Investigation, Writing - review & editing. **Oscar Gomis**: Investigation, Writing - review & editing. **Juan Angel Sans**: Investigation, Writing - review & editing. **K.A. Vanaja**: Investigation, Writing - review & editing. **A.S. Asha**: Investigation, Writing - review & editing. **Catalin Popescu**: Investigation, Writing - review & editing.

Declaration of Competing Interest

The authors declare that they have no known competing financial interests or personal relationships that could have appeared to influence the work reported in this paper.

Acknowledgments

We are thankful for the financial support received from the Spanish Ministerio de Ciencia e Innovación and the Agencia Estatal de Investigación under national projects PGC2018-094417-B-I00 (co-financed by EU FEDER funds), MAT2016-75586-C4-1-P/2-P, FIS2017-83295-P, PID2019-106383GB-C41/C42 and RED2018-102612-T (MALTA Consolider), and from Generalitat Valenciana under project PROMETEO/2018/123. D.S-P, A.O.R, and J.A.S acknowledge financial support of the Spanish MINECO for the RyC-2014-15643, RyC-2016-20301, and RyC-2015-17482 Ramón y Cajal Grants, respectively. Authors thank ALBA-CELLS synchrotron for providing beamtime (ALBA experiments 2012010170).

Author contributions

K.A.V. and A.S.A. synthesized the sample. D.S.P., D.M.G., B.G.D., O.G., J.A.S., and C.P. performed the X-ray diffraction measurements at MSPD beamline in ALBA-CELLS synchrotron. Diffraction data were later analyzed by R.Ch.J, D.S.P., and J.P.P. The ab initio calculations were done by A.O.R. The writing of the manuscript was done by R.Ch.J., D.S.P. and A.O.R, and all the authors contributed to revising it.

References

[1] H. Kawazoe, M. Yasukawa, H. Hyodo, M. Kurita, H. Yanagi, H. Hosono, P-type electrical conduction in transparent thin films of CuAlO2, Nature 389 (1997) 939–942.
[2] K.L. Chopra, S. Major, D.K. Pandya, Transparent conductors—a status review, Thin Solid Films 102 (1983) 1–46.
[3] M. Yu, G. Natu, Z. Ji, Y. Wu, P-type dye-sensitized solar cells based on delafossite CuGaO2 nanoplates with saturation photovoltages exceeding 460 mV, J. Phys. Chem. Lett. 3 (2012) 1074–1078.
[4] I. Suzuki, Y. Iguchi, Ch Sato, H. Yanagi, N. Ohashi, T. Omata, Comprehensive first-principles study of AgGaO2 and CuGaO2 polymorphs, J. Ceram. Soc. Jpn. 127 (2019) 339–347.
[5] S. Ouyang, N. Kikugawa, D. Chen, Z. Zou, J. Ye, A systematical study on photocalatytic properties of AgMO2 (M = Al, Ga, In): effects of chemical compositions, crystal structures and electronic structures, J. Phys. Chem. C 113 (2009) 1560–1566.
[6] A.P. Amrute, G.O. Larrazabal, C. Mondelli, J. Perez-Ramirez, CuCrO2 delafossite: a stable copper catalyst for chlorine production, Angew. Chem. Int. Ed. 52 (2013) 9772–9775.
[7] J. Patzsch, I. Balog, P. Krau, C.W. Lehmann, J.J. Schneider, Synthesis, characterization and p–n type gas sensing behaviour of CuFeO2 delafossite type inorganic wires using Fe and Cu complexes as single source molecular precursors, RSC Adv. 4 (2014) 15348–15355.
[8] Y. Dong, C. Cao, Y.S. Chui, J.A. Zapien, Facile hydrothermal synthesis of CuFeO2 hexagonal platelets/rings and graphene composites as anode materials for lithium ion batteries, Chem. Commun. 50 (2014) 10151–10154.
[9] A. Buljan, P. Alemany, E. Ruiz, Electronic structure and bonding in CuMO2 (M = Al, Ga, Y) delafossite-type oxides: an ab-initio study, J. Phys. Chem. B 103 (1999) 8060–8066.
[10] M.F. Iozzi, P. Vajeeston, R. Vidya, P. Ravindran, H. Fjellvag, Structural and electronic properties of transparent conducting delafossite: a comparison between the AgBO2 and CuBO2 families (B = Al, Ga, In, and Sc, Y), RSC Adv. 5 (2015) 1366–1377.
[11] T. Marqueño, D. Santamaria-Perez, J. Ruiz-Fuertes, R. Chulia-Jordan, J.L. Jordá, F. Rey, C. McGuire, A. Kavner, S. MacLeod, D. Daisenberger, C. Popescu, P. Rodriguez-Hernandez, A. Muñoz, An ultra-high CO_2-loaded silicalite-1 zeolite: structural stability and physical properties at high pressures and temperatures, Inorg. Chem. 57 (2018) 6447–6455.
[12] D. Santamaria-Perez, G. Garbarino, R. Chulia-Jordan, M.A. Dobrowolski, C. Muehle, M. Jansen, Pressure-induced phase transformations in mineral chalcocite, Cu2S, under hydrostatic conditions, J. Alloy. Compd. 610 (2014) 645–650.
[13] T.R. Zhao, X-ray diffraction study of copper iron oxide CuFeO2 under pressures up to 10 GPa, Mater. Res. Bull. 32 (1997) 151–157.
[14] J. Pellicer-Porres, A. Segura, Ch. Ferrer-Roca, A. Polian, P. Munsch, D. Kim, XRD and XAS structural study of CuAlO2 under high pressure, J. Phys. Condens. Matter 25 (2013) 115406.
[15] J. Pellicer-Porres, A. Segura, Ch. Ferrer-Roca, D. Martinez-Garcia, J.A. Sans, E. Martinez, J.P. Itie, A. Polian, F. Baudelet, A. Munoz, P. Rodriguez-Hernandez, P. Munsch, Structural evolution of the CuGaO2 delafossite under high pressure, Phys. Rev. B 69 (2004) 024109.
[16] S. Gilliland, J. Pellicer-Porres, A. Segura, A. Muñoz, P. Rodríguez-Hernández, D. Kim, M.S. Lee, T.Y. Kim, Electronic structure of CuAlO2 and CuScO2 delafossites under pressure, Phys. Status Solidi B 244 (2007) 309–314.
[17] A.B. Garg, A.K. Mishra, K.K. Pandey, S.M. Sharma, Multiferroic CuCrO2 under high pressure: in situ X-ray diffraction and Raman spectroscopic studies, J. Appl. Phys. 116 (2014) 133514.
[18] W.M. Xu, G.K. Rozenberg, M.P. Pasternak, M. Kertzer, A. Kurnosov, L.S. Dubrovinsky, S. Pascarelli, M. Munoz, M. Vaccari, M. Hanfland, R. Jeanloz, Pressure-induced Fe↔Cu cationic valence exchange and its structural consequences: high-pressure studies of delafossite CuFeO2, Phys. Rev. B 81 (2010) 104110.
[19] D. Levy, E. Greenberg, S. Layek, M.P. Pasternak, I. Kantor, S. Pascarelli, C. Marini, Z. Konopkova, G.Kh Rozenberg, High-pressure structural and electronic properties of CuMO2 (M = Cr, Mn) delafossite-type oxides, Phys. Rev. B 101 (2020) 245121.
[20] N.P. Salke, A.B. Garg, R. Rao, S.N. Achary, M.K. Gupta, R. Mittal, A.K. Tyagi, Phase transitions in delafossite CuLaO2 at high pressures, J. Appl. Phys. 115 (2014) 133507.
[21] A.B. Garg, R. Rao, Copper delafossites under high pressure – a brief review of XRD and Raman spectroscopic studies, Crystals 8 (2018) 255.
[22] J. Pellicer-Porres, D. Martínez-García, A. Segura, P. Rodríguez-Hernández, A. Muñoz, J.C. Chervin, N. Garro, D. Kim, Pressure and temperature dependence of the lattice dynamics of CuAlO2 investigated by Raman scattering experiments and ab initio calculations, Phys. Rev. B 74 (2006) 184301.
[23] J. Pellicer-Porres, A. Segura, E. Martínez, A.M. Saitta, A. Polian, J.C. Chervin, B. Canny, Vibrational properties of delafossite CuGaO2 at ambient and high pressure, Phys. Rev. B 72 (2005) 064301.
[24] W. Liu, Q. Liu, Z.-T. Liu, First principles studies of structural, mechanical, electronic, optical properties and pressure-induced phase transition of CuInO2 polymorph, Physica B 407 (2012) 4665–4670.
[25] K.A. Vanaja, R.S. Ajimsha, A.S. Asha, M.K. Jayaraj, p-type electrical conduction in α-AgGaO2 delafossite thin films, Appl. Phys. Lett. 88 (2006) 212103.
[26] H. Nagatani, I. Suzuki, M. Kita, M. Tanaka, Y. Katsuya, O. Sakata, T. Omata, Structure of α-AgGaO2: ternary I-III-VI_2 oxide semiconductor with a wurtzite-derived structure, J. Solid State Chem. 222 (2015) 66–70.
[27] W.C. Sheets, E.S. Stampler, M.I. Beroni, M. Sasaki, T.J. Marks, T.O. Mason, K.R. Poppelmeier, Silver delafossite oxides, Inorg. Chem. 47 (2008) 2696–2705.
[28] R.D. Shannon, D.B. Rogers, C.T. Prewitt, Chemistry of noble metal oxides. I. Syntheses and properties of ABO2 delafossite compounds, Inorg. Chem. 10 (1971) 713–718.
[29] R. Nagarajan, N. Tomar, Ultrasound assisted ambient temperature synthesis of ternary oxide AgMO2 (M = Fe, Ga), Solid State Chem. 182 (2009) 1283–1290.
[30] M. Akhtar, M. Menon, M. Sunkara, G. Sumanasekera, A. Durygin, J.B. Jasinski, High-pressure synthesis of rhombohedral α-AgGaO2 via direct solid state reaction, J. Alloy. Compd. 641 (2015) 87–92.
[31] G.A. Korteweg, L.L. Van Reijen, Magnetic interactions between Fe(III) ions in the solid solutions CuM1-xFexS2 (M = Al, Ga, In) and AgM1-xFexO2 (M = Al, Ga), J. Phys. Chem. Solids 142 (1981) 987.
[32] F. Fauth, I. Peral, C. Popescu, M. Knapp, The new material science powder diffraction beamline at ALBA synchrotron, Powder Diffr. 28 (2013) S360–S370.

[33] A. Dewaele, P. Loubeyre, M. Mezouar, Equations of state of six metals above 94 GPa, Phys. Rev. B Condens. Matter Mater. Phys. 70 (2004) 1–8.
[34] C. Prescher, V.B. Prakapenka, DIOPTAS: a program for reduction of two-dimensional X-ray diffraction data and data exploration, High Press. Res. 35 (2015) 223–230.
[35] J. Rodríguez-Carvajal, Recent advances in magnetic structure determination by neutron powder diffraction, Phys. B Phys. Condens. Matter 192 (1993) 55–69.
[36] G. Nolze, W. Kraus, PowderCell 2.0 for Windows, Powder Diffr. 13 (2016) 256–259.
[37] T.J.B. Holland, S.A.T. Redfern, Unit cell refinement from powder diffraction data: the use of regression diagnostics, Mineral. Mag. 61 (1997) 65–77.
[38] P.E. Blöchl, Projector augmented-wave method, Phys. Rev. B 50 (1994) 17953–17979.
[39] P. Giannozzi, O. Andreussi, T. Brumme, O. Bunau, M. Buongiorno Nardelli, M. Calandra, C. Car, C. Cavazzoni, D. Ceresoli, M. Cococcioni, N. Colonna, I. Carnimeo, A. Dal Corso, S. de Gironcoli, P. Delugas, R.A. DiStasio Jr., A. Ferretti, A. Floris, G. Fratesi, G. Fugallo, R. Gebauer, U. Gerstmann, F. Giustino, T. Gorni, J. Jia, M. Kawamura, H.-Y. Ko, A. Kokalj, E. Küçükbenli, M. Lazzeri, M. Marsili, N. Marzari, F. Mauri, N.L. Nguyen, H.-V. Nguyen, A. Otero-de-la-Roza, L. Paulatto, S. Poncé, D. Rocca, R. Sabatini, B. Santra, M. Schlipf, A.P. Seitsonen, A. Smogunov, I. Timrov, T. Thonhauser, P. Umari, N. Vast, X. Wu, S. Baroni, Advanced capabilities for materials modelling with quantum ESPRESSO, J. Phys. Condens. Matter 29 (2017) 465901.
[40] A.D. Becke, On the large-gradient behavior of the density functional exchange energy, J. Chem. Phys. 85 (1986) 7184–7187.
[41] J.P. Perdew, K. Burke, M. Ernzerhof, Generalized gradient approximation made simple, Phys. Rev. Lett. 77 (1996) 3865–3868.
[42] E.R. Johnson, The exchange-hole dipole moment dispersion model, Non-Covalent Interactions in Quantum Chemistry and Physics, Elsevier, 2017, pp. 169–194 Chapter 5.
[43] A.D. Becke, E.R. Johnson, Exchange-hole dipole moment and the dispersion interaction revisited, J. Chem. Phys. 127 (2007) 154108–154114.
[44] A. Otero-De-La-Roza, E.R. Johnson, Van der Waals interactions in solids using the exchange-hole dipole moment model, J. Chem. Phys. 136 (2012) 174109.
[45] A. Otero-De-La-Roza, E.R. Johnson, Aplication of XDM to ionic solids: the importance of dispersion for bulk moduli and crystal geometries, J. Chem. Phys. 153 (2020) 054121.
[46] A. Otero-De-La-Roza, V. Luaña, Gibbs2: a new version of the quasi-harmonic model code. I. Robust treatment of the static data, Comput. Phys. Commun. 182 (2011) 1708–1720.
[47] A. Otero-De-La-Roza, D. Abbasi-Pérez, V. Luaña, Gibbs2: a new version of the quasiharmonic model code. II. Models for solid-state thermodynamics, features and implementation, Comput. Phys. Commun. 182 (2011) 2232–2248.
[48] A.A. Mostofi, J.R. Yates, Y.-S. Lee, I. Souza, D. Vanderbilt, N. Marzari, Wannier90: a tool for obtaining maximally-localised Wannier functions, Comput. Phys. Commun. 178 (2008) 685.
[49] A. Otero-de-la-Roza, A. Martíin Pendás, E.R. Johnson, Quantitative electron delocalization in solids from maximally localized Wannier functions, J. Chem. Theory Comput. 14 (2018) 4699.
[50] A. Otero-de-la-Roza, E.R. Johnson, V. Luaña, Critic2: a program for real-space analysis of quantum chemical interactions in solids, Comput. Phys. Commun. 185 (2014) 1007.
[51] K.A. Vanaja, R.S. Ajimsha, A.S. Asha, K. RajeevKumar, M.K. Jayaraj, Pulsed laser deposition of p-type α-AgGaO2 thin films, Thin Solid Films 516 (2008) 1426–1430.
[52] R.W.G. Wyckoff, The crystal structure of silver oxide, Am. J. Sci. 3 (1922) 184–188.
[53] P. Niggli, Die Kristallstruktur einiger Oxyde I, Z. Kristallogr. 57 (1922) 253–299.
[54] D. Santamaria-Perez, D. Daisenberger, J. Ruiz-Fuertes, T. Marqueño, R. Chulia-Jordan, C. Muehle, M. Jansen, P. Rodriguez-Hernandez, A. Muñoz, E.R. Johnson, A. Otero-de-la-Roza, Gold(I) sulfide: unusual bonding and an expected computational challenge in a simple solid, Chem. Sci. 10 (2019) 6467–6475.
[55] D. Santamaria-Perez, A. Morales-Garcia, D. Martinez-Garcia, B. Garcia-Domene, C. Muehle, M. Jansen, Structural phase transitions on AgCuS stromeyerite mineral under compression, Inorg. Chem. 52 (2013) 355–361.
[56] L.E. Orgel, Stereochemistry of metals of the B sub-groups. Part I. Ions with filled d-electron shells, J. Chem. Soc. 843 (1958) 4186–4190.
[57] D. Santamaria-Perez, M. Marques, R. Chulia-Jordan, J.M. Menendez, O. Gomis, J. Ruiz-Fuertes, J.A. Sans, D. Errandonea, J.M. Recio, Compression of silver sulfide: X-ray diffraction measurements and total-energy calculations, Inorg. Chem. 51 (2012) 5289–5298.
[58] D. Santamaria-Perez, E. Bandiello, D. Errandonea, J. Ruiz-Fuertes, O. Gomis, J.A. Sans, F.J. Manjon, P. Rodriguez-Hernandez, A. Muñoz, Phase behavior of Ag2CrO4 under compression: structural, vibrational and optical properties, J. Phys. Chem. C 117 (2013) 12239–12248.
[59] D. Santamaria-Perez, T. Marqueño, S. MacLeod, J. Ruiz-Fuertes, D. Daisenberger, R. Chulia-Jordan, D. Errandonea, J.L. Jordá, F. Rey, C. McGuire, A. Mahkluf, A. Kavner, C. Popescu, Structural evolution of CO_2-filled pure silica zeolite under high-pressure high-temperature conditions, Chem. Mater. 29 (2017) 4502–4510.
[60] D. Santamaria-Perez, J. Ruiz-Fuertes, M. Peña-Alvarez, R. Chulia-Jordan, T. Marqueño, D. Zimmer, V. Gutierrez-Cano, S. MacLeod, E. Gregoryanz, C. Popescu, P. Rodriguez-Hernandez, A. Muñoz, Post-tilleyite, a dense calcium silicate-carbonate phase, Sci. Rep. 9 (2019) 7898.
[61] A. Leineweber, R.E. Dinnebier, Anisotropic microstrain broadening of minium, Pb3O4, in a high-pressure cell: Interpretation of line-width parameters in terms of stress variations, J. Appl. Crystallogr. 43 (2010) 17–26.
[62] A.N. Salak, A.L. Zhaludkevich, O.V. Ignatenko, A.D. Lisenkov, A.A. Yaremchenko, M.L. Zheludkevich, M.G.S. Ferreira, High-pressure induced phase formation in the CuGaS2-CuGaO2 chalcopyrite-delafossite system, Phys. Status Solidi B 251 (2014) 1192–1196.
[63] F. Birch, Finite strain isotherm and velocities for single-crystal and polycrystalline NaCl at high pressures and 300 K, J. Geophys. Res. 83 (1978) 1257.
[64] S. Okamoto, S.I. Okamoto, T. Ito, The crystal structure of a new hexagonal phase of AgFeO2, Acta Crystallogr. B 28 (1972) 1774–1777.
[65] S. Ouyang, D. Chen, D. Wang, Z. Li, J. Ye, Z. Zou, From β-phase particle to α-phase hexagonal-platelet superstructure over AgGaO2: phase transformation, formation mechanism of morphology, and photocatalytic properties, Cryst. Growth Des. 10 (2010) 2921–2927.
[66] R.F.W. Bader, A quantum-theory of molecular structure and its applications, Chem. Rev. 91 (1991) 893.
[67] R.F.W. Bader, Molecular fragments of chemical bonds, Acc. Chem. Res. 8 (1975) 34.
[68] A. Bondi, Van der Waals volumes and radii, J. Phys. Chem. 68 (1964) 441.
[69] A. Otero-de-la-Roza, J.D. Mallory, E.R. Johnson, Metallophilic interactions from dispersion-corrected density-functional theory, J. Chem. Phys. 140 (2014) 18A504.
[70] D. Santamaria-Perez, A. Vegas, C. Muehle, M. Jansen, Structural behavior of alkaline sulfides under compression: high-pressure experimental study on Cs2S, J. Chem. Phys. 135 (2011) 054511.
[71] A. Vegas, D. Santamaria-Perez, M. Marques, M. Florez, V.G. Baonza, J.M. Recio, Anions in metallic matrices model: application to the aluminium crystal chemistry, Acta Crystallogr. B 62 (2006) 220–227.